

Improving Hatching Strategies for Powder Bed Based Additive Manufacturing with an Electron Beam by 3D Simulations

Matthias Markl^{a,*}, Regina Ammer^b, Ulrich Rde^b, Carolin Krner^a

^aChair of Metals Science and Technology, WTM, University of Erlangen-Nuremberg, Martensstr. 5, 91058 Erlangen, GERMANY

^bChair for System Simulation, LSS, University of Erlangen-Nuremberg, Cauerstr. 11, 91058 Erlangen, GERMANY

Abstract

This paper extends 3D simulation results of layer hatching process strategies for additive manufacturing by electron beam melting (EBM) applications to exploit the future energy potential of electron guns with higher beam power. The physical model, discretized by a three dimensional thermal lattice Boltzmann method, is briefly presented. The numerical implementation is validated on the basis of an experimental process window up to 1.2kW beam power of hatching a cuboid with a basic, state-of-the-art process strategy, whereby the numerical results are classified into three categories: ‘porous’, ‘good’ and ‘swelling’, depending on the part density and quality of the surface. In this paper we extend and improve the basic process strategy, to use higher beam powers. First, the numerical process window is extended, to determine the limits of this technique. Then we introduce different process strategies of the electron beam to build the part as fast as possible under the restriction of a dense part with a good dimensional accuracy. These process strategies can be used to improve the quality of the parts, reduce the build time and costs, maximize the beam power usage and, therefore, use the full potential of high power electron guns.

Keywords: Powder bed based additive manufacturing, electron beam melting, process strategies, hatching strategies, numerical simulation, thermal lattice Boltzmann method

1. Introduction

Electron Beam Melting (EBM) is a powder bed based Additive Manufacturing (AM) method used to produce metallic structures (Heinl et al., 2007). The great advantage of EBM manufacturing is the construction of strong and flexible structures with a high geometric complexity, which opens new opportunities in many different applications, ranging from aerospace (Rawal et al., 2013) to medical implant (Murr et al., 2011) manufacturing. In contrast to other AM methods, the EBM process produces parts with a sufficient surface and dimensional quality and material properties at relatively low build times (Vayre et al., 2012). However, until today the build is still not sufficiently fast to make it economically viable for less specific, mass production applications. In order to accelerate this technology and to ensure the final quality, numerical simulations are used to improve state-of-the-art process strategies.

We discretize the EBM process with a 3D thermal lattice Boltzmann method (LBM), including physical phenomena, like hydrodynamic flow, capillarity, wetting, as well as beam absorption and phase transformations, but excluding viscous heat dissipation and compressibility and

evaporation effects. In Markl et al. (2013) parallel and optimized 3D absorption algorithms are derived and the description of further modeling aspects are given in Ammer et al. (2014b). The implementation is embedded in the WALBERLA¹ (widely applicable lattice Boltzmann solver from Erlangen) framework, which is a lattice Boltzmann based fluid flow solver with highly parallelized kernels (Feichtinger et al., 2011; Kstler and Rde, 2013), and the *pe*² (Physics Engine) framework (Pickl et al., 2012), which performs the parallel simulation of the powder bed generation.

In Ammer et al. (2014b) the numerical method is validated, while in Ammer et al. (2014a) the validation focuses on single line examples and the basic hatching process strategy, comparing numerical results with experimental data. These results demonstrate the high accordance of the thermal LBM approach to the real EBM process and allows us to analyze and improve different process strategies.

In this paper the numerical examples are extended to higher beam powers. Until now reliable experiments with the basic process strategy are available for different setups, but only up to 1.2kW. The current development of electron guns with higher beam power has reached 4kW (Kornilov et al., 2013) and aims to provide a maximum beam

*Corresponding author. Tel.: +49-9131-8520783

Email address: matthias.markl@fau.de (Matthias Markl)

¹www.walberla.net

²www10.informatik.uni-erlangen.de/de/Research/Projects/pe/

power of at least 10 kW. It is already obvious from current knowledge that state-of-the-art process strategies cannot use this potential advantage, because high evaporation rates and resulting evaporation pressures will destroy the dimensional accuracy of the part.

Therefore, in a first step the numerical process window will be extended with the basic process strategy to determine the maximum usable beam power. Subsequently, two different techniques are simulated to improve the basic process strategy. On the one hand the beam diameter and the scan velocity are increased and on the other hand the line offset is bisected and the scan velocity is doubled. With both strategies the overall build time of the part will decrease, while the maximum beam power increases. This accelerates the process, reduces manufacturing costs and opens the opportunity for a larger variety of parts and applications.

The outline of the article is as follows: In the following section the 3D thermal LBM used for the simulation of the EBM process is described in brief. Subsequently, the numerical simulation setup and classification criteria used for all numerical simulations are defined. In the next section the process window is extended with the basic process strategy and finally the different strategies are described and the numerical results are discussed. Finally, the numerical simulation results are summarized and future research topics outlined.

2. Numerical Method

Thermodynamic fluid transport including phase transitions is modeled by the single phase-continuum conservation equations:

$$\nabla \cdot \mathbf{u} = 0, \quad (1)$$

$$\partial_t \mathbf{u} + (\mathbf{u} \cdot \nabla) \mathbf{u} = -\frac{1}{\rho} \nabla p + \nu \nabla^2 \mathbf{u} + \mathbf{F}, \quad (2)$$

$$\partial_t E + \nabla \cdot (E \mathbf{u}) = \nabla \cdot (k(E) \nabla E) + \Phi, \quad (3)$$

with time t , macroscopic velocity \mathbf{u} , density ρ , hydrostatic pressure p , body forces \mathbf{F} , like the gravity, and kinematic viscosity ν . The thermal diffusivity $k(E)$ is related to the thermal energy density E , depending on the fluid temperature, specific heat capacity and latent heat for phase transitions. Energy sources, like the electron beam, are summarized in Φ . Fluid compression, viscous heat dissipation and evaporation are neglected by this model.

The Navier-Stokes equations (1) and (2) are numerically solved by an isothermal LBM (Higuera and Jimenez, 1989) introduced by McNamara and Zanetti (1988). The idea of LBM is solving the Boltzmann equation in the hydrodynamic limit for a particle distribution function (pdf) in the physical momentum space. A pdf $f(\mathbf{x}, \mathbf{v}, t)$, describes the probability of finding a particle with velocity \mathbf{v} at position \mathbf{x} at time t . The local, macroscopic values of ρ and \mathbf{u} can be evaluated by integration.

Pure, thermodynamic LBM, which additionally solve equation (3), are the multi-speed LBM (Alexander, 1993; Chen et al., 1994) and the multi-distribution approach (Massaioli et al., 1993; Shan, 1997; He et al., 1998). The multi-speed LBM has higher nonlinear velocity terms and is an extension of the isothermal LBM. Even though there exist stabilization techniques (McNamara and Alder, 1995), numerical instabilities are the main disadvantage of these methods. Additionally, only one Prandtl number can be simulated, limiting the range of applications. The multi-distribution LBM avoid these drawbacks using a separate pdf $h(\mathbf{x}, \mathbf{v}, t)$ for the energy density field.

The D3Q19 stencil, a finite set of 19 discrete velocities \mathbf{e}_i with lattice weights ω_i (He and Luo, 1997), discretizes the microscopic space. At each lattice site, mass, momentum and energy transport is modeled by the pdfs f_i and h_i , respectively. The macroscopic quantities are computed by

$$\rho = \sum_i f_i, \quad \rho \mathbf{u} = \sum_i \mathbf{e}_i f_i, \quad E = \sum_i h_i. \quad (4)$$

The collision operator is approximated by the BGK operator (Bhatnagar et al., 1954; Chen et al., 1994),

$$\Omega_f = -\frac{1}{\tau_f} (f_i - f_i^{\text{eq}}) + F_i \quad (5)$$

$$\Omega_h = -\frac{1}{\tau_h(E)} (h_i - h_i^{\text{eq}}) + \Phi_i, \quad (6)$$

where f_i^{eq} and h_i^{eq} is the Maxwell equilibrium distribution (He and Luo, 1997), F_i denotes an external force term (Luo, 2000), like the gravity, and Φ_i is the absorbed energy of the electron beam (Markl et al., 2013). The relaxation times τ_f , τ_h are related to the viscosity ν and the thermal diffusivity $k(E)$, respectively, by

$$\nu = c_s^2 \Delta t (\tau_f - 0.5), \quad k(E) = c_s^2 \Delta t (\tau_h(E) - 0.5). \quad (7)$$

The Maxwell equilibrium distribution is approximated by a Taylor series expansion (He and Luo, 1997) and is given by,

$$f_i^{\text{eq}} = \omega_i \rho \left(1 + \frac{(\mathbf{e}_i \cdot \mathbf{u})}{c_s^2} + \frac{(\mathbf{e}_i \cdot \mathbf{u})^2}{2c_s^4} - \frac{\mathbf{u}^2}{2c_s^2} \right), \quad (8)$$

$$h_i^{\text{eq}} = \omega_i E \left(1 + \frac{(\mathbf{e}_i \cdot \mathbf{u})}{c_s^2} \right). \quad (9)$$

The lattice speed of sound c_s^2 is $c^2/3$ with lattice cell length c and Δt is the time step.

In the incompressible flow limit, i.e. for small Mach numbers, the constitutive equations (1)-(3) can be derived by a Chapman-Enskog expansion (Palmer and Rector, 2000; Chatterjee and Chakraborty, 2006; Shi and Guo, 2009).

Körner et al. (2005) introduce a volume-of-fluid based free surface lattice Boltzmann approach, where the gas and the material phase are separated by a closed interface layer. Each interface cell is partly covered by the

material phase, defined by a fill level. The gas phase is neglected, thus the method only works on the material phase assuming that the thermodynamic behavior is completely covered. Boundary conditions imposed at the interface ensure mass, momentum and energy conservation. Detailed information regarding the free surface boundary conditions used for this LBM model can be found in Ammer et al. (2014b).

3. Simulation Results

In this section we describe the experimental and numerical setup used in Ammer et al. (2014a) to validate the numerical process window. The process window is extended to higher velocities with the basic process strategy to find the maximum usable beam power. Then this process strategy is modified in two ways. First we increase the beam diameter and the scan velocity. Second, the line offset is halved and the scan velocity is doubled.

3.1. Experimental and numerical setup

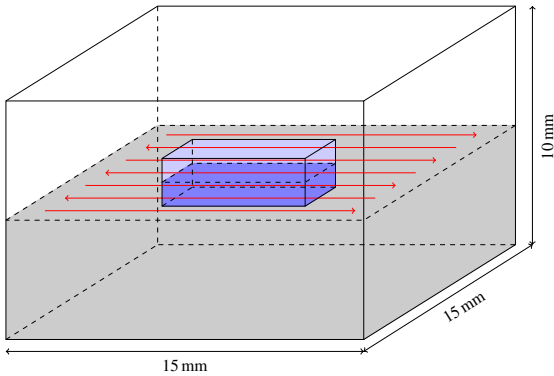


Figure 1: Experimental Setup (gray): A cuboid of $15 \times 15 \times 10 \text{ mm}^3$ is hatched with a line offset of 0.1 mm; Simulation Setup (blue): A cuboid of $1.44 \times 0.64 \times 0.24 \text{ mm}^3$ in the center of the experimental domain hit by seven scan lines is simulated

In the experimental setup a cuboid of $15 \times 15 \times 10 \text{ mm}^3$ is generated by hatching Ti-6Al-4V powder particles with a line offset of 0.1 mm and a layer thickness of 0.05 mm layer by layer (cf. Fig. 1 red arrows). The scanning direction from layer to layer is always perpendicular. The hatching differs by line energy and scan velocity of the electron beam. The line energy E_L is defined by,

$$E_L = \frac{U \cdot I}{v} = \frac{P}{v}, \quad (10)$$

where U denotes the acceleration voltage in [V], I the current in [A] and v the scan velocity in [m/s] of the electron beam. The parameter set (E_L, v) defines the electron beam, whereby the acceleration voltage is fixed to 60 kV. The material solidus and liquidus temperatures are 1878 K and 1934 K, respectively.

The electron beam is modeled by a two-dimensional Gaussian distribution, where we use a standard deviation

of 0.1 mm. The effective diameter is measured as the full width half max (FWHM) value. This is the width of the Gaussian distribution at half of the maximum beam power, which corresponds to 0.235 mm.

Because of the high computational cost of the 3D simulations we only model the hatching of one powder layer instead of the multiple layers. We also minimize the simulated powder particle layer, focusing only a rectangular powder layer of $1.44 \times 0.64 \times 0.24 \text{ mm}^3$ with seven hatching lines inside (cf. Fig. 1). Thus, a beam offset per layer is defined where the electron beam is on but outside the simulated powder particle bed. This simplification is justified by the good agreement of experimental and numerical data (Ammer et al., 2014a). The lattice spacing is $\Delta x = 5 \cdot 10^{-6} \text{ m}$ and the time step is $\Delta t = 1.75 \cdot 10^{-7} \text{ s}$. All other material parameters are directly taken from the properties of Ti-6Al-4V. At the bottom of the simulation domain, a thermal Dirichlet boundary condition (Ginzburg, 2005) with build chamber temperature at 1000 K and a no-slip half-way bounce-back boundary condition are used. In both other dimensions periodic boundary conditions are applied, to influence the melt pool dynamics as little as possible. In order to minimize numerical errors induced by the boundary treatment, all measurements and images cut off the outside regions.

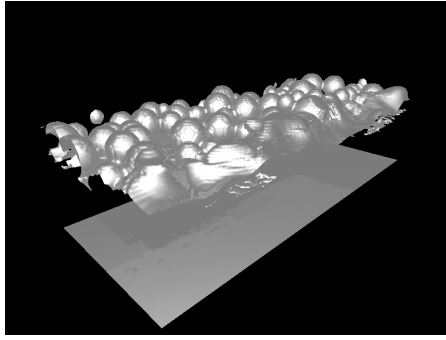
The experimentally generated parts are classified into three groups: ‘porous’, ‘good’ and ‘swelling’. The upper bound for ‘porous’ results is a relative density of 99.5%. If significant bulges on the surface of the part can be detected, then it is categorized into ‘swelling’. All other parts are declared as ‘good’.

Due to the volume of fluid approach, the relative density of the numerical part is easy to measure and uses the same upper bound, but the numerical simulation excludes evaporation effects and no numerical swelling occurs. Therefore, the maximum melt pool temperatures are averaged and if they exceed 7500 K then the result is classified as ‘swelling’ Ammer et al. (2014a). This limit is not comparable with real experiments, because the cooling effect caused by evaporation is not simulated.

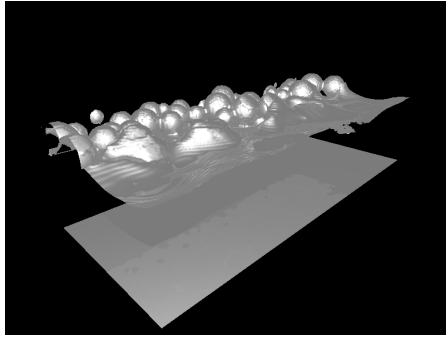
3.2. Maximum Beam Power

In Ammer et al. (2014a) the numerical process window is compared with experimental results up to 6.4 m/s. Here still good results are achievable, hence we can increase the scan velocities to determine the maximum usable beam power.

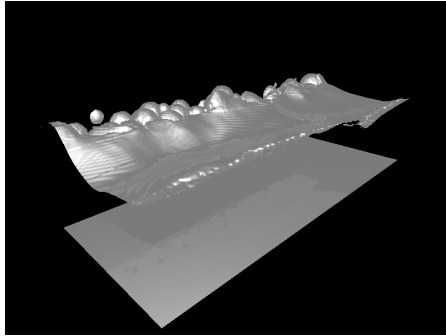
Fig. 2 shows exemplary hatching of one layer with parameter set (0.125 kJ/m, 15 m/s) for four different time steps. The free surface of the powder particles is visualized by an isosurface on the fill level of the interface. In Fig. 2(a) the electron beam scanned one line and the affected powder particles are not yet completely melted. Fig. 2(b) shows the third scanned line by a coming-back electron beam. Here, the particles in the front part of the simulation domain are now melted completely. In Fig. 2(d) the electron beam has scanned seven hatching lines. The



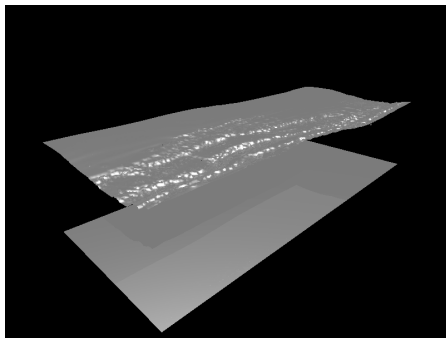
(a) first line scanned



(b) third line scanned



(c) fourth line scanned



(d) seventh line scanned

Figure 2: Hatching of one layer, (0.125 kJ/m, 15 m/s); isosurfaces of the free surface and the bottom plate are shown, whereas the complete region in between is completely filled with material; liquid parts can be identified by a very smooth free surface, whereas solidified parts show grooves

first half of the simulation domain is already resolidified, as can be seen by the grooves on the free surface. They grow each time the melt pool swashes back and the pool edge solidifies. The back part of the simulation domain is still liquid. There are no pores between the bottom plane and the resulting free surface, which additionally characterizes a good densification.

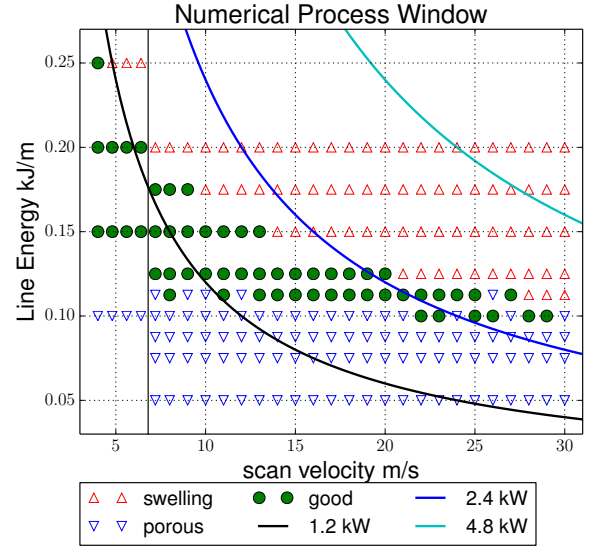


Figure 3: Extended numerical process window with 0.1 mm line offset: up to 6.4m/s the numerical results are in good agreement with experimental data, for higher velocities only numerical data is available due to the limitations of beam power of current EBM machines

Fig. 3 shows the quality of samples with different line energies in [kJ/m] and scan velocities in [m/s] of the electron beam. Porous parameter sets are represented by blue downward triangles, the green circles represent an optimal, good parameter set and the red upward triangles a swelling sample. It can be observed that the higher the scan velocity, the lower the embedded line energy has to be, to get an optimal result.

The left part with up to 6.4 m/s can be compared to the experimental data and shows a good agreement. A detailed discussion of the numerical validation to experimental data is given in Ammer et al. (2014a). Therefore, a tendency of certain strategies can be predicted, which is done here for the basic process strategy by only increasing the scan velocity.

The process window of all green circles is limited by two effects. The upper limit or the evaporation bound is given by the maximum temperature at the surface and is very sharp, i.e., the two different timescales of the beam absorption and the thermal diffusivity lead to a point, where the evaporation rate at the free surface is predictable. In contrast to the evaporation bound, the lower or porosity bound is quite diffuse. This can be seen for 7-12 m/s with a line energy of 0.1125 kJ, where porous and good results flip. Even if the minimum energy to melt a whole layer is deposited into the material, the appearance of the powder

bed has a statistical fluctuation, so there may exist configurations where the heat transfer is adverse and there are resting pores. This is a critical point for a process strategy, because it should lead to reproducible results with low deviations. Therefore, a practical process window will close at approximately 20 m/s with a line energy of about 0.12 kJ. When we compare the resulting beam power of 2.4 kW with the potential of a 10 kW electron gun, then there is still a strong need for further improvements.

3.3. Increasing Beam Diameter

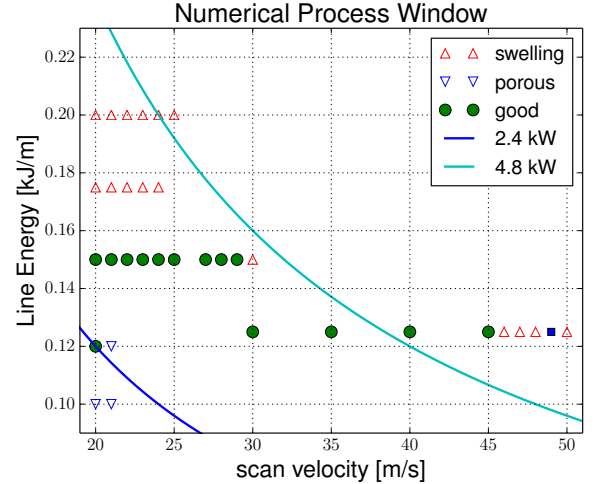
A possible strategy to use a higher beam power is to increase the beam diameter. Then the peak power density at the center of the electron beam decreases, because the energy distribution of the electron beam is nearly a two dimensional Gaussian distribution. This leads to a lower maximum temperature at the surface and to lower evaporation rates and pressures. This strategy decreases the dimensional quality due to a larger melt pool. With the reduced maximum temperatures, we are able to increase line energy and accelerate build velocity by using higher beam powers.

We studied two additional beam shapes with increased effective beam diameters, where the resulting affected area is increased by 50% and 100%. This leads to standard deviations of 0.122 mm and 0.141 mm with a FWHM of 0.287 mm and 0.332 mm, respectively.

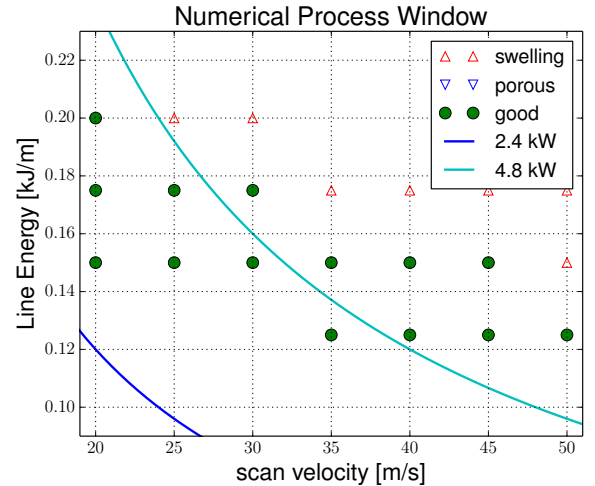
Fig. 4 shows simulation results for both beam diameters. When the beam affected area is increased about 50%, then line energies about 0.125 kW and scan velocities about 40 m/s are predicted, which lead to a total beam power usage up to approximately 5 kW (cf. Fig. 4(a)). When the beam diameter is further increased by 100% (cf. Fig. 4(b)) a higher line energy of about 0.15 kW is applicable, which leads to a total beam power usage of about 6 kW.

These results justify that the potential of 10 kW electron beam guns can be applied with this strategy. Nevertheless, this strategy can cause new challenges, e.g., when thin or very complex geometries are built. The resulting beam diameter lead to a corresponding melt pool width, which is too large to build very thin walls or bridges. Even when the surrounding shape in one layer has fine borders, they cannot be resolved accurately. Even in case of straight borders the dimensional accuracy will decrease with increasing beam diameter. This drawback can be overcome by melting the contour separately, before or after hatching, but then the build time reduction is lost, because the contour has to be melted with a slow and precise beam diameter. Even when using a multi-beam approach, by melting different spots simultaneously, there will be no more benefit in build time.

Summarizing, this strategy is only useful when the hatching regions have a simple geometry, large area and when no additional contour scanning is necessary. In a post-processing step the surface roughness can be further improved.



(a) Increased affected area of 50%



(b) Increased affected area of 100%

Figure 4: Single simulation results with increased beam diameter: Increase of usable beam power up to at least 5 kW and reduction of build time of at least 50%

3.4. Decreasing Line Offset

Another strategy to decrease build time and use higher beam powers is to decrease the line offset of the scan lines. This sounds contradictory, because the overall scan length increases, but it is possible to increase the scan velocity about a higher factor than decreasing the line offset. Here the line offset is bisected and the velocity is doubled to keep the build time constant. Then the line energy is also bisected to keep the used electron beam power constant. This setup is then directly comparable to the basic hatching strategy.

The main idea behind this technique is the re-usage of the deposited energy. The faster the electron beam scans the hatching lines the more local is the deposited energy. Thus, the temperature level stays nearly constant on a high level over the complete scan length with less maximum evaporation rates. Then the material along the

complete scan line becomes liquid and the dynamics of the melt pool changes fundamentally. The movements are no longer aligned with the scan direction, but perpendicular to it. This strategy can be seen like a constant heat source which is distributed on the complete scan length simultaneously.

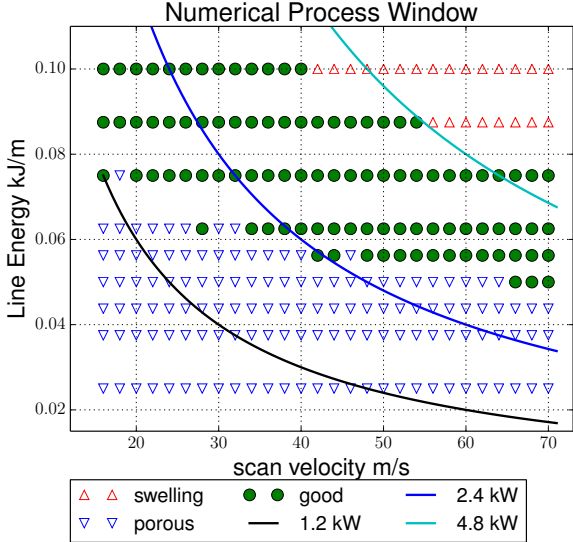


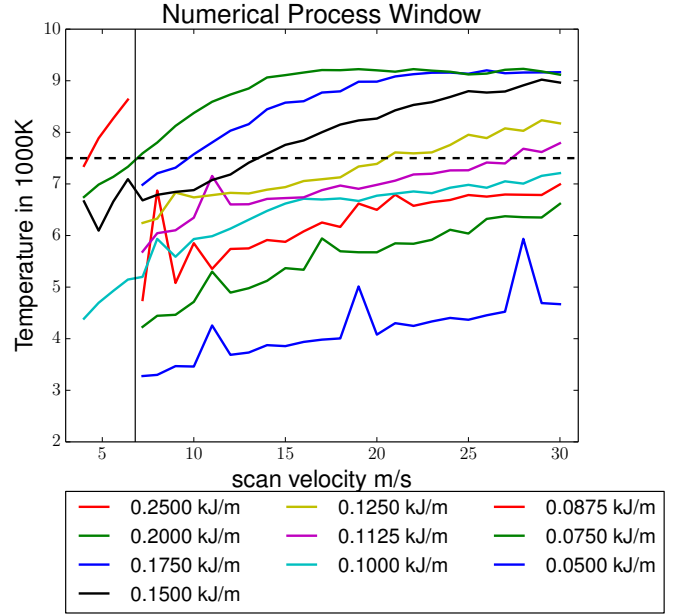
Figure 5: Numerical process window with a scan line offset of 0.05 mm, which possibly allows to use beam powers up to at least 6 kW and reduce the build time by up to 50%

Fig. 5 shows the numerical results for this strategy up to 70 m/s. The upper and lower bound also show the sharp and statistically shaped behavior, respectively. With this strategy the usable beam powers are easily shifted up to 6 kW, like with the increased beam diameters.

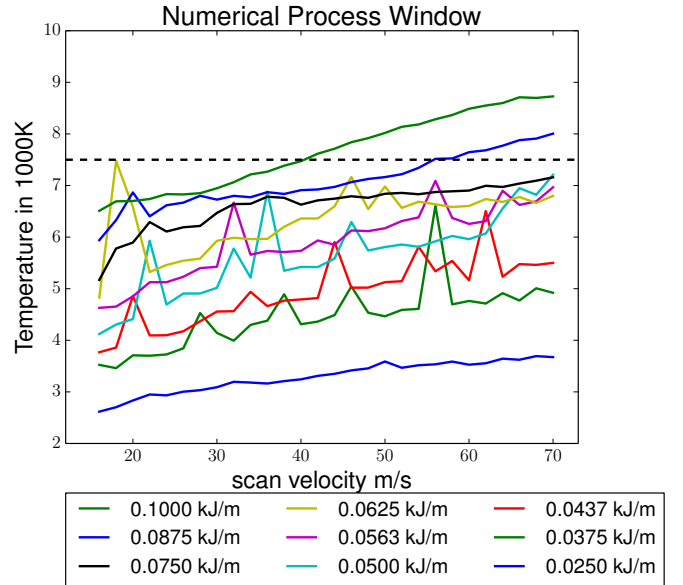
The link to Fig. 3 is found by bisecting the velocity and doubling the line energy, to keep the used beam power and build time constant. Exemplary, when we compare the numerical simulation with good results at (0.1 kJ/m, 20 m/s), which is 2 kW beam power only, with the basic process strategy at (0.2 kJ/m, 10 m/s), we see that this simulation leads to high evaporation rates and no good dimensional accuracy.

Compared to the basic process strategy, this technique spreads the energy of the electron beam over the whole layer more regularly, so that the local maximum temperatures are decreased, but the average temperature over whole scan line is increased. This leads to a larger melt pool, with less dynamics and lower maximum evaporation rates. However, the evaporation rate of the whole free surface may increase due to the larger melt pool which rather affects the composition of the alloy than the dimensional accuracy.

This can be seen directly in Fig. 6, where the maximum temperatures of the current and the basic process strategy are compared. The colored lines are pairwise comparable with the same beam power using the double speed for halved line offset. To stay in a safe regime of the maximum



(a) Maximum temperature with the basic process strategy (0.1 mm line offset): Validated results with experiments are available up to 6.4 m/s



(b) Maximum temperature with decreased line offset strategy (0.05 mm line offset)

Figure 6: Maximum temperatures for basic and decreased line offset strategies: the colored lines are pairwise comparable with the same beam power using doubled speed for bisected line offset. The current strategy decreases the maximum temperatures in comparable simulations.

temperatures for the basic process strategy, a maximum line energy of approximately 0.1 kJ/m can be used with high velocities (cf. Fig. 6(a)). Compared with Fig. 3, we note that there is still a high risk to obtain porous parts.

The small basic process window at comparably low beam powers around 2.4 kW is increased with the new decreasing line offset strategy (cf. Fig. 6(b)). Here line energies of about 0.075 kJ/m can be used safely over a wide range of scan velocities and in comparison to Fig. 5, nearly all simulations lead to dense parts.

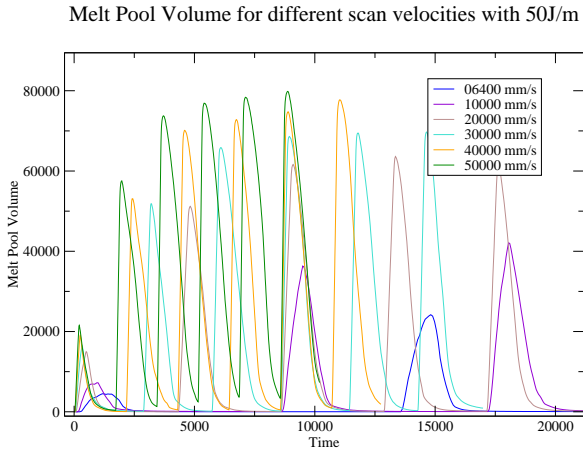


Figure 7: Melt pool volume in cells over the simulation time for different scan velocities with 50 kJ/m: At a scan velocity of 40 m/s the previous scan line is still liquid

The melt pool behavior can be further studied as illustrated Fig. 7, where the melt pool volume in cells of $5 \times 10^{-18} \text{ mm}^3$ depending on the simulation time for different scan velocities with 50 kJ/m is shown. This line energy is chosen, because nearly all simulation results show a relative density up to 99% but are still classified as porous. The melt pool size increases with increasing velocity, whereas the lifetime stays nearly constant. With a higher scan velocity than 40 m/s the previous scan line is still liquid when the electron beam returns. Here it is easy to see that we reuse the deposited energy better with the high scan velocities, because the time durations are so short that the energy cannot dissipate so quickly into the interior of the material.

Summarizing, this strategy increases the width of the process window significantly and leads to more reliable and reproducible processes that have a reduced build time by making use of the high energy potential of the electron beam. The dimensional accuracy is expected to stay the same compared to the basic process strategy, because the beam diameter remains the same.

4. Conclusions

We have presented a numerical method to simulate the EBM process and extended the experimentally validated process window up to higher scan velocities. It has been

shown that the numerical process window for hatching a cuboid with a side length of 15 mm closes at approximately 20 m/s with a line energy of about 0.12 kJ/m. To manufacture multiple parts with equal quality we have to ensure a safety margin from the borders of the process window, which limits the basic process strategy of hatching with 0.1 mm line offset to a maximum beam power of about 2.4 kW.

In order to use the high potential of future electron guns of about 10 kW we studied hatching strategies, where the beam diameter is increased. This technique shows, that the process window can be shifted upwards. Higher beam powers of up to 6 kW can be used with reduced build times of about 50%. However with this strategy, there is still a potential risk that the dimensional accuracy deteriorates. The second hatching strategy bisected the line offset and lead to the same process improvements as the increased beam diameter, with the same quality of densification as the basic process strategy.

Both strategies show, that with modified scan strategies future electron beam powers can be efficiently used to decrease the build time and therefore reduce manufacturing costs and extend the variety of possible applications and parts.

Furthermore, the different strategies have an influence on the microstructure of the final part. By adjusting scan velocity and beam power, the desired microstructure can be adopted. Besides further improvements of enhanced process strategies for hatching and the inclusion of an evaporation model to improve the prediction of swelling, the simulation of the growth of the microstructure is one of the main future research topics.

Acknowledgments

Our work is supported by the European Union Seventh Framework Program – Research for SME’s with full title “High Productivity Electron Beam Melting Additive Manufacturing Development for the Part Production Systems Market” and grant agreement number 286695.

References

- Alexander, F. J., 1993. Lattice Boltzmann thermohydrodynamics. *Physical Review E* 47, R2249– R2252.
- Ammer, R., Markl, M., Jüchter, V., Körner, C., Rüdte, U., 2014a. Validation experiments for LBM simulations of electron beam melting. submitted to *International Journal of Modern Physics C*. URL <http://arxiv.org/abs/1402.2440>
- Ammer, R., Markl, M., Ljungblad, U., Körner, C., Rüdte, U., 2014b. Simulating fast electron beam melting with a parallel thermal free surface lattice Boltzmann method. *Computers & Mathematics with Applications* 67, 318–330.
- Bhatnagar, P., Gross, E., Krook, M., 1954. A model for collision process in gases 1: small amplitude processes in charged and neutral one-component systems. *Physical Review* 50.
- Chatterjee, D., Chakraborty, S., 2006. A hybrid lattice Boltzmann model for solid-liquid phase transition in presence of fluid flow. *Physical Letters A* 351, 359–367.

- Chen, Y., Ohashi, H., Akiyama, M., Oct 1994. Thermal lattice Bhatnagar-Gross-Krook model without nonlinear deviations in macrodynamic equations. *Phys. Rev. E* 50, 2776–2783.
- Feichtinger, C., Donath, S., Köstler, H., Götz, J., Rüde, U., 2011. Walberla: HPC software design for computational engineering simulations. *Journal of Computational Science* 2 (2), 105 – 112.
- Ginzburg, I., 2005. Generic boundary conditions for lattice Boltzmann models and their application to advection and anisotropic dispersion equations. *Advances in Water Resources* 28 (11), 1196–1216.
- He, X., Chen, S., Doolen, G., 1998. A novel thermal model for the lattice Boltzmann method in incompressible limit. *Journal of Computational Physics* 146, 282 – 200.
- He, X., Luo, L.-S., Jun 1997. A priori derivation of the lattice Boltzmann equation. *Phys. Rev. E* 55, R6333–R6336.
- Heinl, P., Rottmair, A., Körner, C., Singer, R., 2007. Cellular titanium by Selective Electron Beam Melting. *Advanced Engineering Materials* 9 (5), 360–364.
- Higuera, F., Jimenez, J., 1989. Boltzmann approach to lattice gas simulations. *Europhysics Letters* 9.
- Körner, C., Thies, M., T.Hofmann, Thürey, N., Rüde, U., 2005. Lattice Boltzmann model for free surface flow for modeling foaming. *Journal of Statistical Physics* 121, 179–196.
- Kornilov, S., Rempe, N., Beniyash, A., Murray, N., Hassel, T., Ribton, C., 2013. On the beam parameters of an electron gun with a plasma emitter. *Technical Physics Letters* 39 (10), 843–846.
- Köstler, H., Rüde, U., 2013. The cse software challenge - covering the complete stack. it - Information Technology Methoden und innovative Anwendungen der Informatik und Informationstechnik 55 (3), 91–96.
- Luo, L.-S., 2000. Theory of the lattice Boltzmann method: Lattice Boltzmann models for non-ideal gases. *Physical Review E* 62, 4982–4996.
- Markl, M., Ammer, R., Ljungblad, U., Rüde, U., Körner, C., 2013. Electron beam absorption algorithms for electron beam melting processes simulated by a three-dimensional thermal free surface lattice Boltzmann method in a distributed and parallel environment. *Procedia Computer Science* 18 (0), 2127 – 2136, 2013 International Conference on Computational Science.
- Massaioli, F., R.Benzi, Succi, S., 1993. Exponential tails in two-dimensional rayleigh-bénard convection. *Europhysics Letters* 21, 305.
- McNamara, G., Alder, B., 1995. Stabilization of thermal lattice Boltzmann methods. *J. Stat. Phys.* 81, 395.
- McNamara, G., Zanetti, C., 1988. Use of the Boltzmann equation to simulate lattice-gas automata. *Physical Review Letters* 61.
- Murr, L., Amato, K., Li, S., Tian, Y., Cheng, X., Gaytan, S., Martinez, E., Shindo, P., Medina, F., Wicker, R., 2011. Microstructure and mechanical properties of open-cellular biomaterials prototypes for total knee replacement implants fabricated by electron beam melting. *Journal of the Mechanical Behavior of Biomedical Materials* 4 (7), 1396–1411.
- Palmer, B., Rector, D., 2000. Lattice Boltzmann algorithm for simulating thermal flow in compressible fluids. *Journal of Computational Physics* 161, 1–20.
- Pickl, K., Götz, J., Iglberger, K., Pande, J., Mecke, K., Smith, A.-S., Rüde, U., 2012. All good things come in threes – three beads learn to swim with lattice Boltzmann and a rigid body solver. *Journal of Computational Science* 3 (5), 374 – 387.
- Rawal, S., Brantley, J., Karabudak, N., June 2013. Additive manufacturing of Ti-6Al-4V alloy components for spacecraft applications. In: *Recent Advances in Space Technologies (RAST), 2013 6th International Conference on.* pp. 5–11.
- Shan, X., 1997. Simulation of rayleigh-bénard convection using a lattice Boltzmann method. *Physical Review E* 55, 2780–2788.
- Shi, B., Guo, Z., Jan 2009. Lattice Boltzmann model for nonlinear convection-diffusion equations. *Phys. Rev. E* 79, 016701.
- Vayre, B., Vignat, F., Villeneuve, F., 2012. Metallic additive manufacturing: State-of-the-art review and prospects. *Mechanics and Industry* 13 (2), 89–96.